RSC Applied Interfaces

ROYAL SOCIETY OF CHEMISTRY

PAPER

View Article Online
View Journal | View Issue

Cite this: *RSC Appl. Interfaces*, 2026, **3**, 539

Dual-function catalysis: linking photo- and electrocatalytic behavior in In_2O_3/TiO_2 composites

Hanna Maltanava,[a] Nikita Belko, *[a] Pauliina Nevalainen,[b] Niko M. Kinnunen,[c] Konstantin Tamarov, [d] Jani O. Moilanen, [e] Jari T. T. Leskinen, [d] Vesa-Pekka Lehto [d] and Polina Kuzhir[a]

Received 7th October 2025,
Accepted 2nd February 2026

DOI: 10.1039/d5lf00304k

rsc.li/RSCApplInter

Efficient catalysts for both photo- and electrocatalytic applications are essential for sustainable technologies. The combination of In_2O_3 and TiO_2 offers tunable structural and electronic properties, supporting multifunctional catalytic applications. We prepare nanostructured In_2O_3/TiO_2 composites with varying oxide ratios and at different temperatures. The resulting powders and thin films are thoroughly characterized to assess their structure, crystallinity, and surface area. Photocatalytic activity depends strongly on composition, with 70–90 wt% TiO_2 samples showing the highest enhancement in hydroxyl radical generation and rhodamine B degradation, attributed to increased specific surface area and improved charge separation. In oxygen electroreduction, catalytic activity increases for TiO_2 and In_2O_3 as the annealing temperature rises from 200 to 450 °C. Formation of composites between the two oxides does not result in a significant inprovement in electrocatalytic activity. These findings highlight the potential of In_2O_3/TiO_2 systems as tailored and multifunctional catalysts for environmental remediation and energy conversion.

1 Introduction

The development of advanced nanocomposite catalysts is essential for overcoming the limitations of current energy conversion and environmental technologies, which often depend on expensive, scarce, or inefficient materials. To enable scalable and sustainable solutions, nanocatalysts must be cost-effective, stable, and highly active under practical conditions. In this context, materials that exhibit both photo- and electrochemical functionality are particularly valuable. Furthermore, catalysts capable of operating efficiently in both domains can unlock synergistic effects, enhance overall performance, and broaden their applicability across diverse energy and environmental platforms. Photocatalysis enables the use of solar energy for driving chemical reactions, while electrocatalysis offers precise control over reaction pathways in systems such as fuel cells and water electrolyzers. The photochemical and electrochemical processes are interfacial reactions, involving the transfer of charge carriers toward reactants or intermediate species at the interface of a catalyst and a liquid phase. Therefore, improving the charge separation efficiency and interfacial activity of photogenerated charge carriers is the primary objective in the field of photo(electro) catalysis. Moreover, both types of reactions are multi-stage processes with several competing reduction products, which presents challenges in terms of low energy efficiency and limited chemical selectivity. The investigation of electrochemical processes, in particular the oxygen reduction reaction (ORR), can serve as a useful basis for understanding the mechanisms and dynamics of photocatalytic reactions, allowing for a more in-depth study of their efficiency and optimization.

ORR has attracted significant attention for the development of efficient catalysts and support materials. ORR is a key process in energy devices such as fuel cells, photoelectrochemical converters, and lithium–air batteries,[1,2] but its inherently slow kinetics require highly active and stable electrodes.[3] Platinum and its alloys remain the benchmark for ORR due to their excellent catalytic activity,[4–6] yet their high cost and limited availability hinder large-scale deployment.[3] This has driven the search for alternative materials, particularly transition metal oxides, which show promising activity in alkaline media.[7,8] Ideal candidates must combine high electrical conductivity, chemical stability, large surface area, and low cost.[7,9]

Indium oxide (In_2O_3) has attracted considerable attention in recent years for its diverse applications in photo- and

[a] *Department of Physics and Mathematics, University of Eastern Finland, Joensuu, Finland. E-mail: nikita.belko@uef.fi*
[b] *Department of Chemistry and Sustainable Technology, University of Eastern Finland, Joensuu, Finland*
[c] *Lappeenranta University of Technology, School of Engineering Science, Department of Separation Science, Lappeenranta, Finland*
[d] *Department of Technical Physics, University of Eastern Finland, Kuopio, Finland*
[e] *Department of Chemistry, Nanoscience Centre, University of Jyväskyla, Jyväskyla, Finland*

electrocatalysis. It is frequently employed as support material or as a component in composite catalysts due to its favorable electronic properties and structural tunability.

Electrocatalytic applications of this material have been demonstrated in multiple works. For instance, In_2O_3 has been used as a support for Pt nanoparticles in electrocatalytic ORR, both in its pristine form[10] and doped with Sn.[11] IrO_x@In_2O_3 heterostructures[12] and La^{3+}-doped In_2O_3 nanostructures[13] have shown enhanced performance in oxygen evolution reaction. Pristine In_2O_3 and its composite with carbon dots have demonstrated efficient $2e^-$ oxygen electroreduction to H_2O_2,[14] while tubular In_2S_3@In_2O_3 structures have shown dual functionality in photocatalytic H_2O_2 production and decomposition.[15] In_2O_3-based heterostructures with Cu_2O and reduced graphene oxide have been applied in photocatalytic degradation of methylene blue, reduction of Cr^{6+}, and the oxygen evolution reaction.[16] Various heterostructures of In_2O_3 have been employed for CO_2 electroreduction, including composites with ceria and zirconia,[17] In/In_2O_3,[18] Cu-doped In_2O_3 with carbon black,[19] V-doped In_2O_3 nanocrystals,[20] and In_2O_3@C/graphene nanocomposites.[21]

Photocatalytic applications of In_2O_3 are equally diverse. In_2O_3/In_2S_3 microsphere heterostructures have been used for photocatalytic nitrogen fixation,[22] while In_2O_3 nanostructures with various morphologies have been applied for the degradation of persistent pollutants such as perfluorooctanoic acid, with hydroxyl radical generation identified as a key reactive intermediate.[23,24] Comparative studies have also evaluated the photocatalytic performance of In_2O_3 micro- and nanostructures in methyl violet decolorization.[25] Complex heterostructures such as SnO_2/Pt/In_2O_3 have been used for photocatalytic hydrogen evolution and degradation of 2,4-dichlorophenol.[26]

The photoelectrochemical properties of In_2O_3 have been explored as well, with nanocubes exhibiting significant photocurrent generation.[27]

Despite recent progress, the intrinsic catalytic properties of In_2O_3 and its function as a support material remain underexplored. Nevertheless, the growing interest in In_2O_3-based heterostructures and composites has spurred a surge in research focused on their photo- and electrocatalytic applications.[28,29] Among these, In_2O_3/TiO_2 composites are particularly appealing due to the tunability of the structure and phase composition of TiO_2 as well as its versatility as a photo- and electrocatalyst.[30] However, only a limited number of studies have investigated the catalytic potential of this oxide combination. Specifically, In_2O_3/TiO_2 heterostructures have been employed for the photocatalytic degradation of 2-chlorophenol[31] and rhodamine B,[32] as well as for hydrogen evolution reaction.[33] Ternary heterostructures incorporating In_2O_3, TiO_2, and g-C_3N_4 have also been reported for hydrogen evolution reaction and rhodamine B degradation.[34] There is even less information on electrocatalytic and photoelectrocatalytic behavior of In_2O_3/TiO_2 composites.[35,36] These findings highlight the need for a comprehensive investigation of the photo- and electrocatalytic properties of In_2O_3/TiO_2 heterostructures, as well as their interplay. Such studies would be instrumental in optimizing synthesis strategies and catalytic performance and could pave the way for employing these composites as supports for other active materials, such as noble-metal nanoparticles.

In this work, we report a simple sol–gel-based synthesis of In_2O_3/TiO_2 composite materials with tunable composition and structure. The resulting powders and thin films are characterized using transmission electron microscopy (TEM), scanning electron microscopy (SEM), X-ray diffractometry (XRD), X-ray photoelectron spectroscopy (XPS), and N_2 physisorption measurements to evaluate their morphology, crystallinity, and specific surface area. The photocatalytic performance of the powders is then tested in hydroxyl radical generation and rhodamine B (RhB) degradation, and the electrocatalytic activity of the thin films is examined in the ORR in an alkaline medium. By correlating the photo- and electrocatalytic behavior with composition, annealing temperature, and structural characteristics, we identify key factors for tailoring the composites to specific applications.

2 Experimental

2.1 Materials

$In(NO_3)_3$·4.5 H_2O (>98%), $TiCl_4$ (99.9%), HNO_3 (70%), ammonia solution (25%), KOH (>90%), RhB (>95%), α-(4-pyridyl *N*-oxide)-*N*-*tert*-butylnitrone (POBN, 95%), and terephthalic acid (TA, >98%) were purchased from Merck. All solutions were prepared in deionized (DI) water.

2.2 Synthesis of catalysts

$In(OH)_3$ hydrosol was prepared by dissolving 27.48 g $In(NO_3)_3$·4.5 H_2O in 190 mL DI water, yielding a 10% solution. A 12.5% aqueous ammonia solution (100 mL) was added dropwise (*ca.* 1 drop in 2 seconds) to the $In(NO_3)_3$ solution in an ice bath with stirring until the pH value reached 8. The resulting sol was centrifuged at 2500 rpm and washed with DI water five times. Then, 0.99 mL concentrated HNO_3 was added to the washed $In(OH)_3$ precipitate. The precipitate turned into a turbid white liquid. The sol was sonicated with an ultrasonic horn (22 kHz) until it turned into a transparent gel. The gel turned back into a sol after cooling down to room temperature. The concentration (solid content) of $In(OH)_3$ in the sol was found to be 23 wt%.

TiO_2 hydrosol was prepared by hydrolyzing $TiCl_4$ as described in our previous work.[37]

Powdered catalysts were prepared by lyophilizing the sols of $In(OH)_3$ and TiO_2 sols and their mixtures containing 50, 70, and 90 wt% TiO_2. The lyophilized powders were then annealed in air at 200, 300, or 450 °C for 2 h. Thin film electrodes were prepared by spin coating of the sols of $In(OH)_3$ and TiO_2 and their mixtures containing 25, 50, and 75 wt% TiO_2 onto titanium plates. The samples were then heated at 170 °C for 20 min to adhere the films to the substrate surface. Spin coating with subsequent heating were repeated 4 times to reach the desired film thickness. Finally,

the samples were annealed in air at 200, 300, or 450 °C for 1 h. In the following, the samples are denoted as "In_2O_3-*T*", "TiO_2-*T*", and "In_2O_3/TiO_2(*x*)-*T*", where *T* is the temperature and *x* is the weight percentage of TiO_2.

2.3 Characterization

XRD patterns were acquired with a PANalytical Empyrean diffractometer using CuKα-radiation at a scanning speed of 0.4° min^{-1}. The identification of diffraction peaks was carried out using reference data from the Joint Committee on Powder Diffraction Standards (JCPDS).[38]

XPS spectra were acquired using a Nexsa G2 spectrometer (Thermo Fisher Scientific Inc.). Measurements were carried out with a 400 μm X-ray spot size (Al K-α radiation) and concurrent operation of an electron flood gun in charge compensation mode. Low-resolution survey spectra were initially collected (pass energy: 200 eV; step size: 1 eV; dwell time: 10 ms), followed by automatic identification of the elements. Subsequently, selected peaks were recorded in the high-resolution mode (pass energy: 50 eV; step size: 0.1 eV; dwell time: 50 ms). These high-resolution spectra were subjected to peak fitting, performed using Avantage v6.9 software (Thermo Fisher Scientific Inc.). Peak fitting employed the Avantage smart background and variable peak components, each modeled as a Gaussian–Lorentzian product mixture (30% Lorentzian).

For SEM and TEM measurements, aqueous suspensions of the prepared powders were deposited on silicon and formvar/carbon supported copper grids (Sigma-Aldrich, 930253), respectively. SEM imaging was conducted with a Zeiss LEO 1550 scanning electron microscope in the secondary electron detection mode at an accelerating voltage of 10 kV. TEM imaging was performed using a Jeol JEM-2100F microscope operating at an accelerating voltage of 200 kV.

Measurements of specific surface area were conducted using a Microtrac Belsorp MAX X device. Before measurement, a sample was pretreated at 150 °C for 2 h. N_2 gas physical adsorption occurred at the liquid nitrogen temperature. After completing physical adsorption, the desorption of N_2 gas was recorded as well. Specific surface areas were obtained from the physical adsorption data by applying Brunauer–Emmett–Teller (BET) theory.

2.4 EPR spectroscopy

Photocatalytic production of OH radicals by the prepared catalysts was tested using EPR spectroscopy with spin trapping. X-band EPR spectra of trapped radicals were recorded with a Magnettech MiniScope MS 200 spectrometer. The following parameters were applied for all samples: microwave frequency ~9.4 GHz, center field 3349 G, spectral width 99 G, scan time 60 s, and modulation amplitude 1000 mG. The concentration of catalyst powders was 2.5 mg mL^{-1}. POBN was used as a spin trap at a concentration of 50 mM. To convert OH radicals into 1-hydroxyethyl radicals, which were subsequently trapped by POBN, 5 vol% EtOH was added to the samples.[39,40] The mixtures were sealed in 50 μL glass capillaries and irradiated for 3 minutes with an LED peaking at 385 nm, with an irradiance of 14 mW cm^{-2}. EPR spectra were recorded both before and after irradiation to assess the influence of radiation.

2.5 Photocatalytic activity

$OH^{\bullet}$ production was also registered with TA as described in ref. 37. In brief, TA was dissolved in 0.1 M KOH and then diluted 10-fold with DI water resulting in a solution containing 3 mM TA and 10 mM KOH. The catalysts in powdered form were dispersed in the TA solution at 1 mg mL^{-1} by sonicating for 3 min. The suspensions were irradiated with a light-emitting diode (LED) peaking at 385 nm, with an irradiance of 60 mW cm^{-2}. During irradiation, the suspensions were agitated with a magnetic stirring bar. After irradiation, the catalysts were removed from the TA solution by centrifuging at 14 000 rpm for 15 min. Finally, the fluorescence spectra of the supernatants were recorded under 310 nm excitation using an Edinburgh FLS1000 spectrofluorimeter (2 × 1.5 nm excitation and emission slits). The fluorescence intensity of 2-hydroxyterephthlic acid, the product of TA oxidation by OH radical, peaking at 425 nm was used as a measure of $OH^{\bullet}$ production.

Photocatalytic activity of the prepared powders was also tested by quantifying the degradation of RhB as a model environmental pollutant. A 2.5 mM stock solution of RhB was prepared in a 50 vol% aqueous ethanol. The stock solution was then diluted with DI water to a final concentration of 10 μM. The catalysts in powdered form were dispersed in the RhB solution at 1 mg mL^{-1} by sonicating for 3 min. The suspensions were irradiated with a light-emitting diode (LED) peaking at 365 nm, with an irradiance of 150 mW cm^{-2}. During irradiation, the suspensions were agitated with a magnetic stirring bar. After irradiation, the catalysts were removed from the RhB solution by centrifuging at 14 000 rpm for 15 min. Finally, the absorption spectra of the supernatants were recorded using a PerkinElmer Lambda 900 spectrophotometer. The peak absorbance at 555 nm was extracted and used to quantify the degradation of RhB.

The photocatalytic measurements were repeated three times, and the mean values and standard deviations were calculated (error bars in Fig. 9 represent the standard deviations).

2.6 Electrocatalytic activity

The electrocatalytic activity of the thin films prepared on titanium was tested in the ORR using electrochemical techniques. Cyclic voltammograms, linear sweep voltammograms, and potentiostatic chronoamperometry curves were recorded using an Autolab PG-STAT 302 N potentiostat/galvanostat at room temperature. The potential sweep rates in cyclic and linear sweep voltammetry was 10 mV s^{-1}. Chronoamperometry was performed at −0.8 V for TiO_2 and In_2O_3 and at −0.9 V for In_2O_3/TiO_2. The measurements were conducted in a single-compartment glass cell equipped with three electrodes. The reference electrode was an Hg/HgO electrode filled with 1 M KOH, and the counter electrode was a Pt foil. The potential of the reference electrode was 115 mV *vs.* a saturated calomel electrode. A 0.1 M aqueous KOH solution

served as a supporting electrolyte and was saturated with O_2 gas for 1 h before the measurements. In cyclic voltammetry and chronoamperometry experiments, the TiO_2, In_2O_3 and In_2O_3/TiO_2 films deposited onto Ti plates served as the working electrodes. The area of the working electrodes was 1 cm^2. Linear sweep voltammograms were recorded on a Ti rotating disc electrode (RDE) with deposited oxide films. The area of the RDE was 0.14 cm^2. The rotational frequency of the electrode was varied between 1000 and 5000 RPM. The Levich equation was used to determine the number of electrons transferred in the ORR reaction.[41]

3 Results

3.1 Characterization of the prepared powders and films

The morphology of TiO_2, In_2O_3 powders, and In_2O_3/TiO_2 composites synthesized at 300 °C was examined using TEM (Fig. 1). All samples consisted of nanoparticles aggregated into micron-sized clusters. TiO_2 powder featured particles predominantly 5–10 nm in size, with most exhibiting spherical or near-spherical shapes. In contrast, In_2O_3 powder contained particles ranging from 7 to 20 nm, including a notable fraction of elongated particles.

In the In_2O_3/TiO_2 composites, the particle size was primarily around 5 nm. However, particles approximately 10 nm in size and smaller particles of 2–3 nm were also observed. The latter are presumed to be TiO_2 nanocrystallites, suggesting that the presence of In_2O_3 may inhibit TiO_2 nanocrystallite growth. This interpretation is further supported by the XRD analysis presented below. TEM micrographs of higher resolution, demonstrating the crystalline nature of the nanoparticles, are shown in Fig. S1.

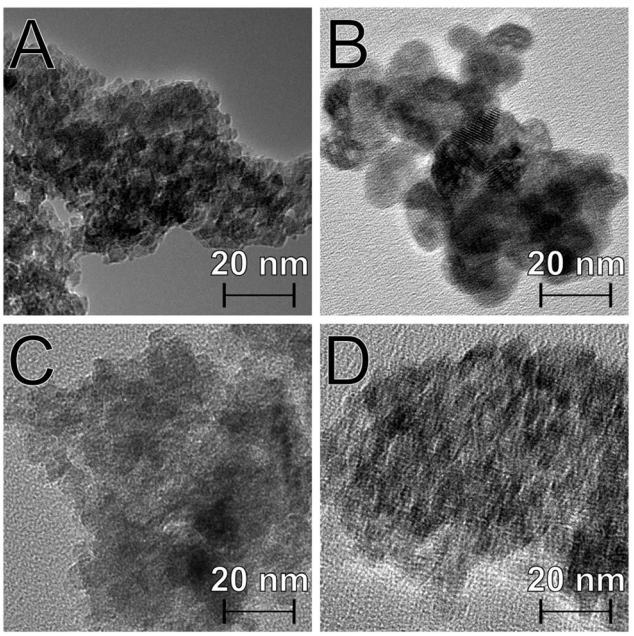

Fig. 1 TEM micrographs of the prepared powders: TiO_2-300 (A), In_2O_3-300 (B), In_2O_3/TiO_2(30)-300 (C), and In_2O_3/TiO_2(90)-300 (D).

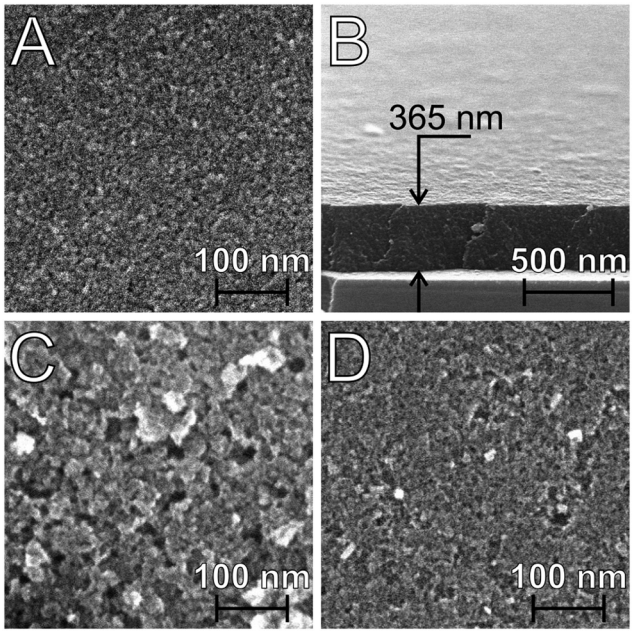

Fig. 2 SEM micrographs of the prepared thin films: TiO_2-200 (A), cross section of TiO_2-200 (B), In_2O_3-200 (C), and In_2O_3/TiO_2(75)-200 (D).

Uniform thin films were fabricated by spin-coating the precursor sols onto Ti substrates. Subsequent thermal treatment induced the formation of nanocrystalline TiO_2, In_2O_3, and In_2O_3/TiO_2 composite films exhibiting a mesoporous structure (Fig. 2). SEM micrographs reveal well-defined nanopores, with average pore diameters of approximately 5 nm for TiO_2 and 15 nm for In_2O_3. The pore sizes for the In_2O_3/TiO_2(75)-200 composite were intermediate between those for the individual oxides. The final film thickness ranged between 350 and 400 nm.

Crystallization and phase transition processes in the powders were studied using XRD (Fig. 3, Tables S1 and S2). XRD patterns of xerogels obtained by drying pure TiO_2 sol at

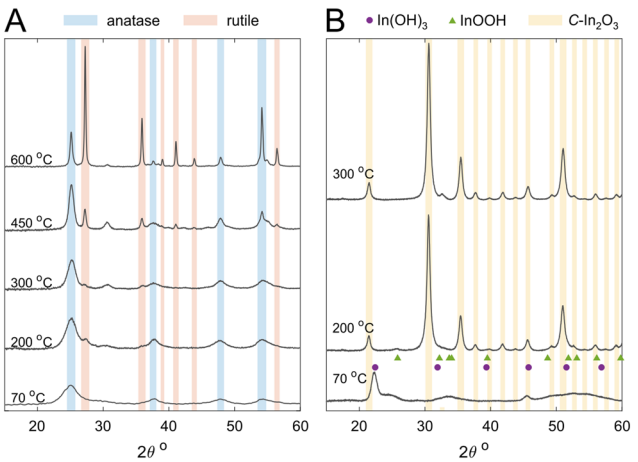

Fig. 3 XRD patterns for TiO_2 (A) and In(OH)3 (B) powders prepared at different temperatures. Assignment of the XRD reflexes is provided in Tables S1 and S2.

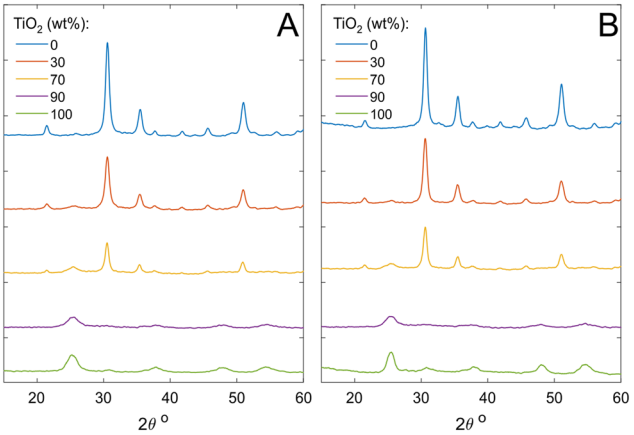

Fig. 4 XRD patterns for In_2O_3/TiO_2 composites with different oxide ratios annealed at 200 °C (A) and 450 °C (B).

70 °C indicated the formation of nanocrystalline anatase. Thermal treatment promoted the growth of anatase crystallites, with the anatase-to-rutile phase transition progressing with the increase in annealing temperature. According to previously reported data, anatase-to-rutile transformation is completed at temperatures above 700 °C.[35] TiO_2 powders annealed at 200 and 300 °C consisted primarily of anatase, with minor rutile admixture (Fig. 3A). Average crystallite sizes were calculated using the Debye–Scherrer equation based on the full width at half maximum of the diffraction peaks, with the shape factor assumed to be 0.9. The crystallite size of anatase was found to be 4.5 nm at 200 °C and increased to 9 nm after calcination at 300 °C. These values are consistent with TEM measurements (see Fig. 1), although the particles observed by TEM might contain several nanocrystallites.

The XRD analysis also revealed that the $In(OH)_3$ sol dried at 70 °C is largely amorphous, with only a minor presence of the cubic $In(OH)_3$ phase (Fig. 3B and Table S2). Upon heating to 200 °C, the xerogel predominantly transformed into cubic In_2O_3, accompanied by a small amount of InOOH. Annealing at 300 °C resulted in a complete conversion to the In_2O_3 phase (Fig. 3B).

XRD analysis of In_2O_3/TiO_2 composites annealed at 200 °C and 450 °C revealed no additional crystalline phases beyond those present in the individual xerogels (Fig. 4). This observation suggests that chemical interaction between In_2O_3 and TiO_2 within this temperature range is rather weak.

In the individual oxide xerogels, crystallite sizes increased with temperature—from 4.5 to 34 nm for TiO_2 and from 11 to 17 nm for In_2O_3 as the annealing temperature rose from 200 to 600 °C. In contrast, the growth of anatase crystallites in the binary xerogels was significantly inhibited, as indicated by the pronounced broadening of diffraction peaks (Fig. 4). For instance, in the In_2O_3/TiO_2(90)-600 composite, the average anatase crystallite size remained below 7 nm.

Chemical composition and bonding states in the prepared oxide samples were analyzed using XPS (Fig. 5). In 3d spectra for pure In_2O_3 annealed at 300 °C revealed peaks at binding energies of 445.0 and 452.6 eV, corresponding to In $3d_{5/2}$ and In $3d_{3/2}$, respectively. The peaks are shifted upward in binding energy by ~0.5 eV compared to previously reported data for In_2O_3, possibly due to the presence of a small amount of $In(OH)_3$ on the surface.[42] Additionally, O 1 s spectrum for In_2O_3-300 exhibited components peaking at 530.5 and 532.3 eV, ascribed to oxygen in In_2O_3 and $In(OH)_3$, respectively.

Ti 2p spectra for pure TiO_2 annealed at 300 °C revealed components with binding energies of 458.8 and 464.5 eV, corresponding to Ti $2p_{3/2}$ and Ti $2p_{1/2}$ peaks of octahedrally coordinated Ti^{4+} in TiO_2.[37] The O 1 s peaks located at 530.2 eV and 532.0 eV were assigned to lattice oxygen in TiO_2 and hydroxyl groups (Ti–OH), respectively.

Composite samples In_2O_3/TiO_2(70)-300 and In_2O_3/TiO_2(90)-300 demonstrated In 3d, Ti 2p, and O 1 s spectra, similar to

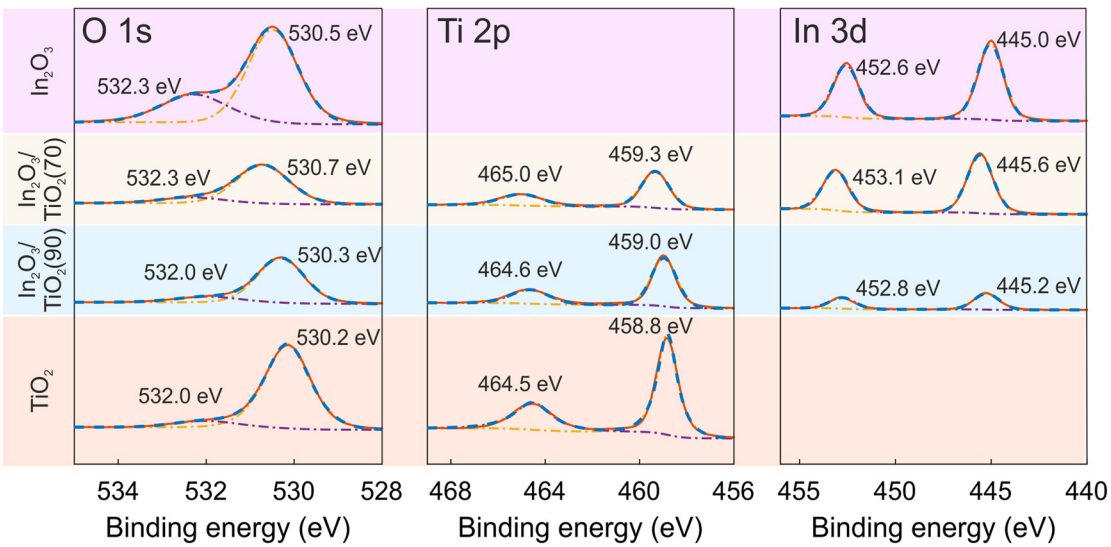

Fig. 5 O 1 s, Ti 2p, and in 3d XPS spectra for In_2O_3, In_2O_3/TiO_2(70), In_2O_3/TiO_2(90), and TiO_2 powders annealed at 300 °C.

those of the individual oxides. However, In 3d and Ti 2p peaks of In_2O_3/TiO_2(70)-300 were shifted to higher binding energies by ~0.5 eV with respect to the individual oxides, possibly due to the formation Ti–O–In bonds or changes in coordination.

Thus, the main effects observed upon increasing temperature were changes in crystallinity as well as transformation of anatase into rutile and $In(OH)_3$ into In_2O_3. The described samples can be considered thermally stable within the described temperature range. This is corroborated by previously reported thermogravimetric analysis of sol–gel TiO_2, In_2O_3, and their composites.[35] The weight loss up to 240 °C was shown to stem from the removal of adsorbed and structural water. At higher temperatures, the weight loss gradually stopped.

The effects of annealing temperature and In_2O_3/TiO_2 ratio on the structural properties of the synthesized powders were further examined using N_2 adsorption–desorption measurements. The specific surface areas of the individual oxides and their composites are presented in Fig. 6. For all compositions, an increase in annealing temperature from 200 °C to 300 °C resulted in a noticeable decrease in surface area, likely due to crystallite growth and partial pore collapse. Pure In_2O_3 exhibited relatively low surface areas (~50 m^2 g^{-1}), while TiO_2 samples showed significantly higher values—185 m^2 g^{-1} for TiO_2-200 and 108 m^2 g^{-1} for TiO_2-300. Remarkably, all composite samples displayed surface areas exceeding those of the corresponding pure oxides prepared at the same temperature. In particular, the In_2O_3/TiO_2(70)-200 composite achieved a surface area as high as 236 m^2 g^{-1}. These findings align well with the TEM and XRD analyses, further corroborating that mutual inhibition of crystallite growth occurs when TiO_2 and In_2O_3 are combined. This interaction likely contributes to the enhanced surface area observed in the composites.

Additional information on the structure of the prepared powders was gained through the analysis of their N_2 adsorption–desorption isotherms. Different types of isotherms were observed across the samples, reflecting differences in pore structure.[43] More specifically, TiO_2-200 exhibited a type I isotherm, characteristic of microporous materials (Fig. 7), while TiO_2-300 showed a type IV isotherm with an H_2a-type hysteresis loop at P/P_0 = 0.4–0.7, indicative of mesoporous solids with a uniform pore size distribution. Additionally, the presence of micropores in TiO_2-300 was evident from the steep uptake at $P/P_0 < 0.1$. In_2O_3 samples annealed at 200 and 300 °C also displayed type IV isotherms with hysteresis loops, confirming their mesoporous nature (Fig. 7). The isotherm types for the composites varied with preparation conditions. Most composite samples exhibited three types of pores: micropores (sharp uptake at $P/P_0 < 0.1$), mesopores (hysteresis at P/P_0 = 0.4–0.8), and macropores (sharp uptake at $P/P_0 > 0.9$).

These N_2 physisorption results suggest that both the oxide ratio and annealing temperature significantly influence the nanoscale structure of In_2O_3/TiO_2 composites, enabling precise control over surface characteristics through synthetic tuning.

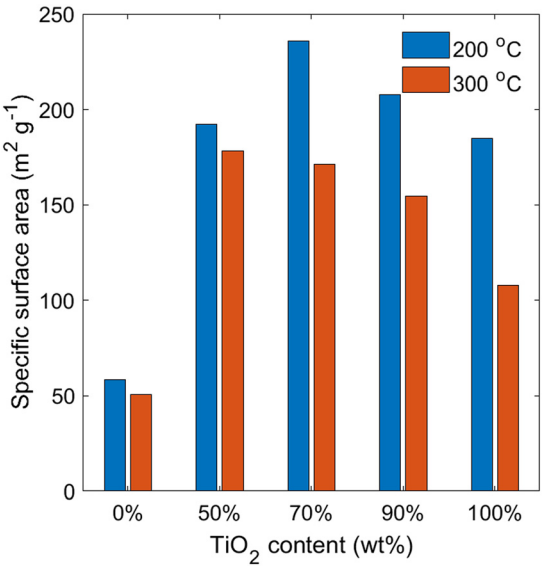

Fig. 6 Specific surface areas of the prepared powders determined from N_2 adsorption–desorption isotherms.

3.2 Photocatalytic activity

The photocatalytic performance of the synthesized materials was assessed based on their ability to generate hydroxyl radical under near-UV irradiation (385 nm). Hydroxyl radical is among the most potent oxidizing species,[44] capable of degrading a wide range of environmental pollutants, including persistent ones.

Photocatalytic $OH^{\bullet}$ production was first detected using EPR with spin trapping. POBN was used as a spin trap. Samples also contained EtOH to convert hydroxyl radical to 1-hydroxyethyl radical before trapping.[39,40] No EPR signal was detected before irradiation for any of the catalysts. Upon irradiation, all samples exhibited similar EPR spectra consisting of three doublets on narrow lines (Fig. 8). The hyperfine splitting constants were a_N = 1.57 mT and a_H = 0.26–0.27 mT. These values agree with literature data for the POBN adduct with the 1-hydroxyethyl radical,[45] which is formed upon the oxidation of EtOH by hydroxyl radicals. Thus, all catalysts demonstrate $OH^{\bullet}$ production upon photoactivation. The hydroxyl radicals may appear through either a reductive pathway from H_2O_2 or an oxidative pathway from OH^-.[46]

$OH^{\bullet}$ production was also measured using TA as a fluorogenic probe. Select fluorescence spectra reflecting $OH^{\bullet}$ production can be seen in Fig. S2. As shown in Fig. 9A, the powders annealed at 200 °C and 300 °C exhibited comparable $OH^{\bullet}$ production efficiencies. The relative amounts of In_2O_3 and TiO_2 had a pronounced effect on photocatalytic activity. Pure In_2O_3 and TiO_2 powders produced similar levels of $OH^{\bullet}$. Notably, the In_2O_3/TiO_2(70)-200 composite demonstrated a two-fold enhancement in $OH^{\bullet}$ generation compared to the individual oxides. However, the same composite annealed at 300 °C showed no significant improvement, performing similarly to the pure phases. Composites containing 90 wt% TiO_2, regardless of annealing temperature, exhibited a marked increase in photocatalytic activity. In contrast, samples with 50 wt% TiO_2 consistently underperformed relative to the pure oxides.

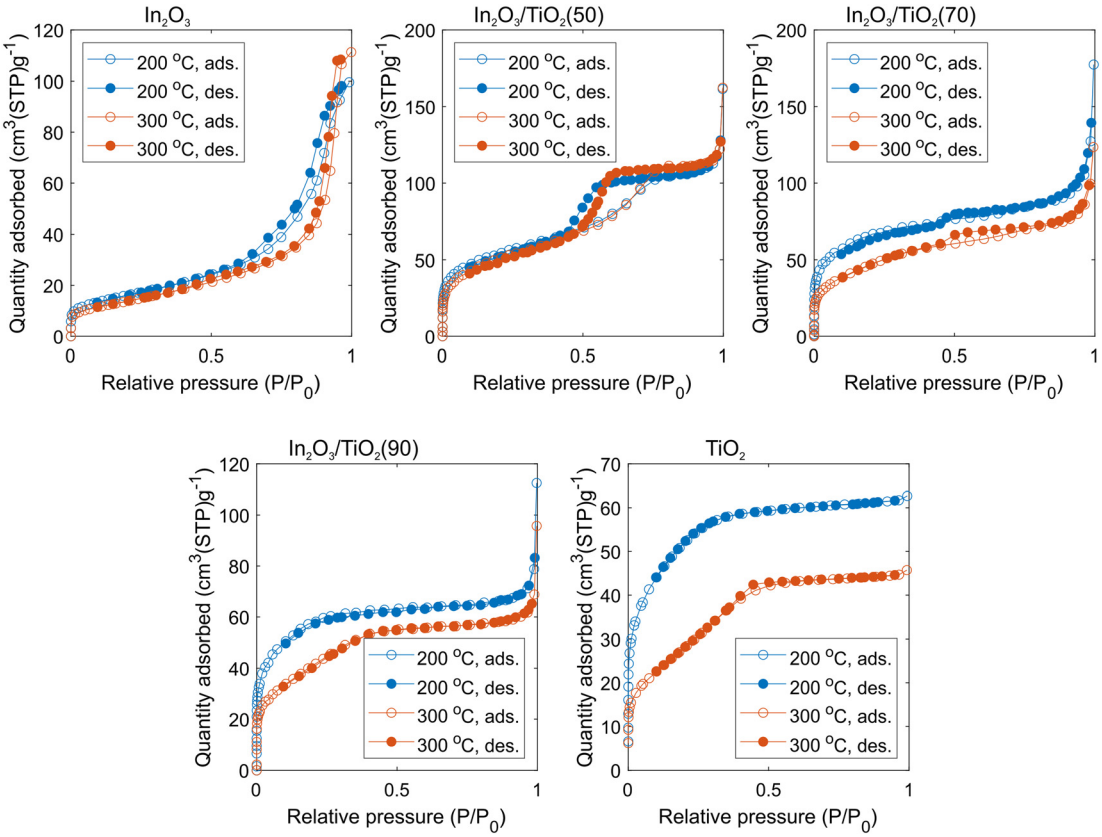

Fig. 7 N_2 adsorption (empty circles) and desorption (filled circles) isotherms of the oxide powders prepared at 200 °C (blue circles) and 300 °C (red circles).

The prepared catalysts were then evaluated for their ability to degrade RhB, a well-known environmental pollutant,[47] under near-UV irradiation (365 nm). The amount of RhB in solution was tracked using spectrophotometry, with select absorption spectra shown in Fig. S3.

The amounts of degraded RhB are summarized in Fig. 9B. In the absence of a photocatalyst, only minor degradation of the dye (~6%) was observed. In contrast, the presence of the synthesized catalysts significantly enhanced the degradation efficiency. Depending on the specific catalyst used, 20–85% of RhB was degraded after 20 min of irradiation (corresponding to a light dose of 180 J cm^{-2}), demonstrating excellent photocatalytic activity across all mesoporous powders.

Notably, composite samples annealed at 200 and 300 °C exhibited similar photocatalytic performance, with all composites outperforming the individual oxides. The highest efficiency was observed for samples containing 70 wt% TiO_2, achieving degradation rates 2–4 times higher than those of pure In_2O_3 or TiO_2.

The degradation of RhB by the catalysts was well fitted by pseudo first-order kinetics (Fig. S4). The reaction constant (k_1) for TiO_2-200 was 0.012 min^{-1} and increased to 0.035 min^{-1} for TiO_2-300. These values are comparable to previously reported data for mesoporous TiO_2 and Degussa P25.[48] A reverse trend was observed for In_2O_3, with samples annealed at 200 and 300 °C showing k_1 values of 0.023 and 0.012 min^{-1}, respectively. The In_2O_3/TiO_2(70) composites annealed at 200 and 300 °C demonstrated rate constants of 0.07 and 0.05 min^{-1}, respectively.

The observed photocatalytic activity (Fig. 9) generally correlated with the specific surface area (Fig. 6), with In_2O_3/TiO_2 composites exhibiting higher surface areas than the individual oxides. However, notable discrepancies were observed. For instance, samples prepared at 200 °C consistently showed larger surface areas than those with the same oxide ratio annealed at 300 °C, yet this trend was not consistently reflected in their photocatalytic performance. These findings suggest that while specific surface area plays a significant role in enhancing photocatalytic activity, it is not the sole determining factor. A balance between surface area, crystallinity, and phase composition appears to be critical for optimizing photocatalytic performance of these composite systems.

The enhanced photocatalytic activity of In_2O_3/TiO_2 composites containing 70 or 90 wt% TiO_2 can be attributed to several factors. First, these samples possess a high specific surface area, which is likely to provide more active sites for dye adsorption, facilitating more efficient degradation. Second, previous studies have shown that a contact between semiconductors with different conduction and valence band edge energies can enhance charge separation, resulting in improved photocatalytic performance.[49] Earlier work[35]

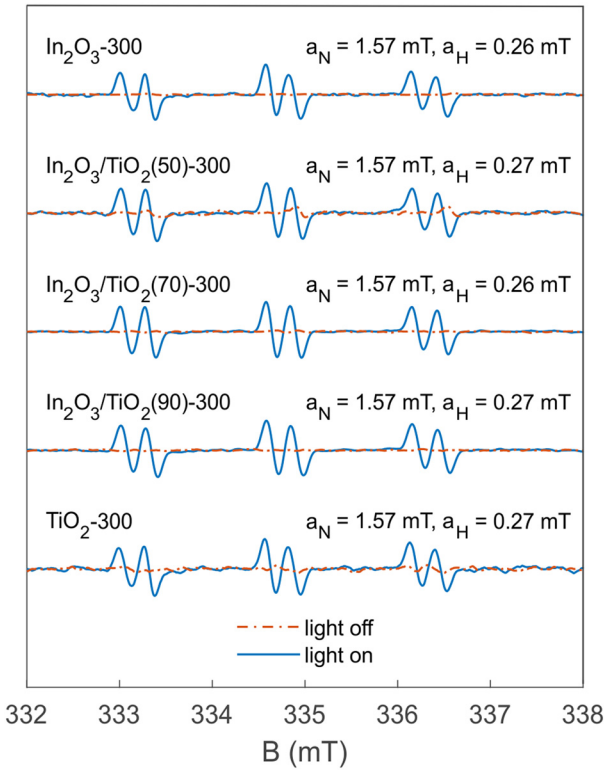

Fig. 8 Normalized EPR spectra for the oxide catalysts annealed at 300 °C, measured in the presence of 50 mM POBN and 5 vol% EtOH before (red dash-dotted lines) and after (blue solid lines) irradiation. The light dose amounted to 2.5 J cm^{-2}. Hyperfine splitting constants for each spectrum are shown in the figure.

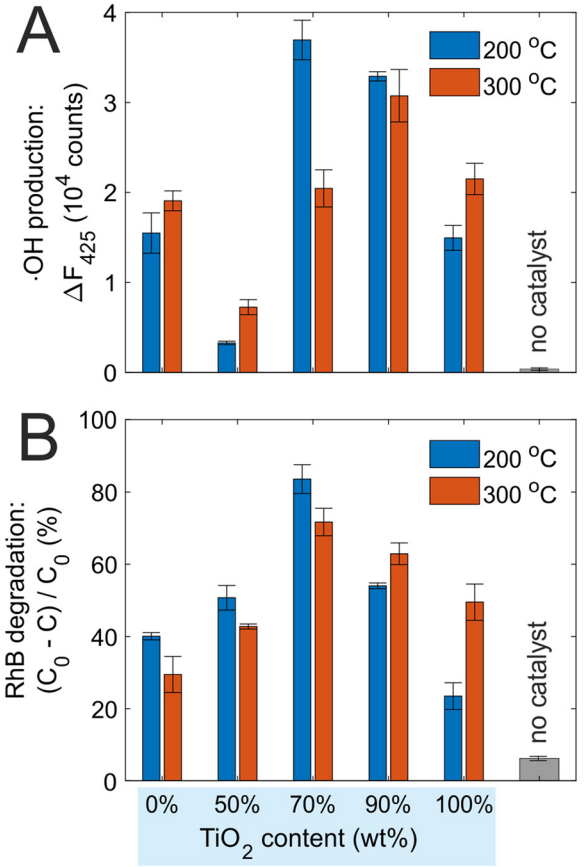

Fig. 9 Photocatalytic activity of TiO_2, In_2O_3, and In_2O_3/TiO_2 powders annealed at 200 and 300 °C. A. Hydroxyl radical production registered using TA as a probe after irradiation with a light dose of 36 J cm^{-2}. B. Photodegradation percentage of RhB after irradiation with a light dose of 180 J cm^{-2}.

demonstrated that nanocrystalline TiO_2 and In_2O_3 films have similar band gaps but different flat-band potentials. This allows photogenerated electrons in TiO_2 to transfer to the lower-lying conduction band of In_2O_3, while holes accumulate in the TiO_2 phase. Such charge separation enables electrons to reduce molecular oxygen and holes to oxidize water molecules or OH^-, leading to the formation of $OH^•$ radicals. These radicals can mineralize organic pollutants into non-toxic products such as CO_2, H_2O, or low-molecular-weight organic acids. This enhanced charge separation and increased $OH^•$ production could explain the improved RhB photodegradation observed in the In_2O_3/TiO_2 composites.

In ref. 50, rhombohedral In_2O_3 nanocrystals were prepared by annealing solvothermally synthesized InOOH nanocrystals and demonstrated degradation of 95% RhB after 4 h of reaction. In ref. 48, Degussa P25 TiO_2 and sol–gel TiO_2 annealed at 400 °C showed k_1 values of 0.018 and 0.022 min^{-1} in RhB degradation, respectively. Degussa P25 TiO_2 modified with phosphorous acid exhibited a RhB degradation percentage of almost 80% after irradiation for 150 min.[51] Hydrothermally prepared anatase TiO_2 nanoparticles demonstrated a k_1 of 0.07 min^{-1} in RhB photodegradation.[52] TiO_2/In_2O_3 nanotube arrays were fabricated by anodization of titanium followed by solvothermal doping with In_2O_3 and reached a RhB degradation percentage of 77% after 2 h of illumination, twice as efficient as bare TiO_2 nanotubes.[53] In_2O_3/TiO_2 heteroarchitectures fabricated by combining electrospinning with a solvothermal process demonstrated over 90% of RhB removal after 4 h of irradiation.[32] Sol–gel In_2O_3/TiO_2 powders described in the current work also exhibit high photocatalytic activity with a k_1 of 0.07 min^{-1} and dye removal percentage of over 80% after 20 min of reaction for In_2O_3/TiO_2(70)-200. However, these comparisons should be treated with care, as experimental conditions (concentrations of catalysts and RhB, wavelength and power of irradiation) vary between different studies.

3.3 Electrocatalytic activity

The electrocatalytic performance of TiO_2, In_2O_3, and In_2O_3/TiO_2 composite thin films toward the ORR in alkaline solution was investigated using cyclic voltammetry (Fig. 10). For TiO_2 films annealed at 200 °C, a characteristic increase in cathodic current was observed at potentials below −0.8 V, indicating the onset of ORR. Two distinct cathodic waves were identified at −0.98 V and −1.20 V. Upon increasing the annealing temperature to 300 °C, the first wave shifted

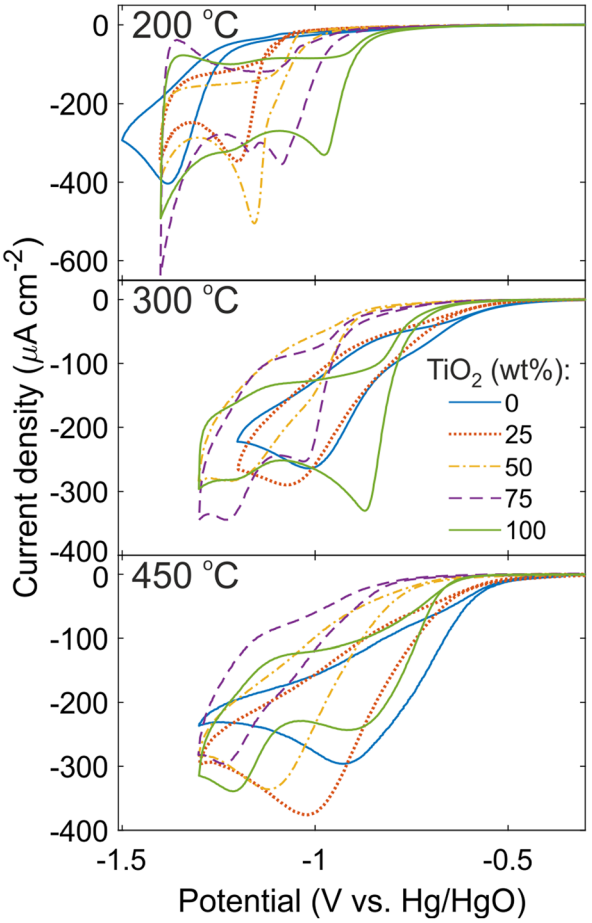

Fig. 10 Cyclic voltammograms for the ORR on TiO_2, In_2O_3, and In_2O_3/TiO_2 electrodes with different oxide ratios annealed at 200, 300, and 450 °C.

anodically to −0.87 V. Annealing at 450 °C resulted in a broader first wave centered at −0.92 V. Notably, the position of the second wave around −1.20 V remained largely unaffected by the annealing temperature.

In contrast, the In_2O_3 film annealed at 200 °C exhibited a single ORR wave at −1.38 V. Increasing the annealing temperature to 300 °C and 450 °C led to a progressive anodic shift of this wave to −1.01 V and −0.92 V, respectively.

The In_2O_3/TiO_2 composites containing 25, 50, and 75 wt% TiO_2 and annealed at 200 °C displayed ORR waves located between those of the pure oxides. The composites annealed at 300 °C and 450 °C exhibited cathodic shifts in ORR wave positions relative to the individual oxide films.

Tafel plots conctructed from the cyclic voltammograms were also analyzed (Fig. S5). For In_2O_3 and TiO_2 annealed at 200 °C, the Tafel slopes were −648 and −255 mV dec^{-1}, respectively. Increasing the annealing temperature significantly reduced these values, reaching −158 mV dec^{-1} for In_2O_3 and −88 mV dec^{-1} for TiO_2 annealed at 450 °C. The In_2O_3/TiO_2 composites prepared at 200 °C exhibited intermediate slopes relative to the individual oxides. At 300 °C, the Tafel slopes for the composites were slightly higher than those of the pure oxides, whereas at 450 °C, the trend reversed.

The RDE method coupled with the Levich equation[41] was used in an attempt to determine the number of electrons (n) transferred in the ORR reaction. Linear sweep voltammograms recorded on an RDE demontrated a continuous increase in current as the potential was swept from −0.1 to −1.3 V. The n values were close to 4 for a TiO_2 film (Fig. S6) and varied between 4 and 5 for an In_2O_3 film (Fig. S7). These findings indicate that the main product of the ORR reaction is likely H_2O. However, the limiting current was not reached in these measurements, probably due to the overlap of several current waves and side reactions such as hydrogen evolution. Strictly speaking, the Levich equation cannot be applied to this system, and the presented n values should be treated with care.

The stability of In_2O_3, TiO_2, and In_2O_3/TiO_2(50) electrodes annealed at 450 °C was assessed using cyclic voltammetry and potentiostatic chronoamperometry (Fig. S8). During repeated potential sweeps between 0.1 and −1.1 V (20 cycles), a substantial decrease in current was observed during the first several cycles, along with slight changes in the position and shape of the ORR waves. Upon further cycling, only minor changes were observed. Similarly, the chronoamperograms demonstrated a rapid decrease in current during the first ~5 min, followed by a stabilization of the current. As the rapid initial current drop was likely due to the consumption of the adsorbed O_2 molecules, the electrodes can be considered reasonably stable under polarization.

Importantly, the onset potential of the ORR measured in this study *via* cyclic voltammetry correlates well with the photocurrent onset potential (E_{on}) previously reported for TiO_2, In_2O_3, and their composites.[35] E_{on} serves as an indicator of the conduction band edge position and reflects the energy of electrons involved in reduction processes, including the ORR. For example, an In_2O_3/TiO_2 composite with 75 wt% TiO_2 prepared at 450 °C exhibited a more negative E_{on} than both pure TiO_2 and other composites prepared at that temeprature. In contrast, an In_2O_3/TiO_2 composite with 25 wt% TiO_2 showed E_{on} approximately 0.15 V more positive than that of TiO_2.[35] Furthermore, increasing the annealing temperature of In_2O_3 from 200 to 450 °C resulted in a positive shift in E_{on} by approximately 0.6 V.[54]

The complex electrochemical behavior of In_2O_3/TiO_2 composites in the ORR can be attributed to the interplay between composition and structure, which governs charge carrier transport and potential distribution under polarization. In nanostructured films, electron transport occurs primarily *via* the hopping mechanism, where grain boundaries between nanocrystals act as barriers to charge transfer.

Conductivity measurements[35] indicate that in composites annealed at 450 °C, charge transport predominantly proceeds through In_2O_3 particles, which exhibit significantly lower internal resistance than TiO_2. When the In_2O_3 content reaches 50 wt% in composites prepared at 450 °C, a sharp increase in conductivity is observed, attributed to the percolation threshold and the formation of interconnected three-dimensional In_2O_3 nanoparticle networks. In contrast, In_2O_3 films annealed at 200 °C display much higher

resistivity due to poor crystallinity and a high density of surface hydroxyl groups, which hinder electron hopping between nanocrystals. As a result, in composites annealed at 200 °C, electron transport from the substrate to the electrode surface occurs predominantly through TiO_2 nanoparticles. The composites annealed at 300 °C propably demonstrate In_2O_3-mediated electron transport. The achievement of percolation threshold and the formation of an In_2O_3 network observed at higher content of In_2O_3 can be explained by a strong inhibition of crystallite growth.

4 Discussion

The dual functionality of In_2O_3/TiO_2 composites in both photocatalytic and electrocatalytic processes underscores the complex interplay between their structural, electronic, and surface characteristics. Photocatalytic activity—evaluated through $OH^{\bullet}$ radical generation and RhB degradation—was found to be highly dependent on the In_2O_3/TiO_2 ratio and annealing temperature. Composites containing 70–90 wt% TiO_2 exhibited significantly enhanced photocatalytic performance compared to the individual oxides.

In contrast, electrocatalytic performance in the ORR followed a different trend. Increasing the annealing temperature resulted in an anodic shift of the ORR peaks and a drop in Tafel slopes. Among the samples annealed at 200 °C, pure TiO_2 and In_2O_3 performed the worst and the best, respectively, while their composites demonstrated intermediate performance. Among the samples annealed at 300 °C, the composites slightly outperformed the pure oxides in terms of Tafel slopes, while at 450 °C, the trend reversed.

These contrasting behaviors underscore that photo- and electrocatalytic processes exhibit both shared and distinct characteristics. Factors such as surface area, catalytic site availability, oxygen adsorption, and band edge positions influence both types of processes. However, photocatalysis is particularly sensitive to charge separation between the two phases, whereas electrocatalysis is more strongly affected by the intrinsic conductivity of the oxide nanoparticles and the formation of percolating conductive networks. Understanding these influences is essential for the rational design of multifunctional catalysts tailored for specific energy and environmental applications.

Conclusions

This work presents a systematic study of the structural, photocatalytic, and electrocatalytic properties of nanocrystalline TiO_2, In_2O_3, and their composites in the form of powders and thin films. Hydrosols of TiO_2 and $In(OH)_3$ were synthesized and combined at various ratios, followed by thermal treatment at different temperatures. This straightforward preparation method enabled precise control over the oxide composition and allowed tuning of crystallinity, phase composition, and specific surface area. Structural characterization revealed that the incorporation of In_2O_3 effectively suppressed TiO_2 crystallite growth and stabilized the anatase phase, even at elevated temperatures—features that contributed to enhanced surface area and photocatalytic performance.

Photocatalytic activity, evaluated through hydroxyl radical generation and RhB degradation, was significantly improved in In_2O_3/TiO_2 composites compared to the individual oxides. The highest activity was observed for composites containing 70–90 wt% TiO_2, attributed to increased surface area and efficient charge separation at the oxide interface.

Electrocatalytic performance in the ORR also showed a strong dependence on composition and annealing temperature. Increasing annealing temperature resulted in a substantial decrease in Tafel slopes, while the formation of composites barely provided an improvement in the electrocatalytic activity. The onset potentials of the ORR correlated well with previously reported photocurrent onset potentials, suggesting a shared influence of conduction band edge alignment on both photo- and electrochemical reactivity.

These findings emphasize the importance of optimizing structural and electronic properties to tailor catalytic performance for specific applications. The In_2O_3/TiO_2 composites developed in this study offer a versatile platform for photo- and electrocatalytic applications, including pollutant degradation, fuel cells, and supports for noble-metal catalysts. Their ease of synthesis, compositional tunability, and dual functionality make them attractive candidates for future sustainable catalytic technologies.

Author contributions

Hanna Maltanava: conceptualization, data curation, investigation, methodology, visualization, writing – original draft. Nikita Belko: conceptualization, data curation, investigation, methodology, visualization, writing – original draft. Pauliina Nevalainen: data curation, investigation, methodology, visualization. Niko M. Kinnunen: data curation, investigation, methodology, visualization, writing – review & editing. Konstantin Tamarov: data curation, investigation, methodology, visualization, writing – review & editing. Jani O. Moilanen: investigation, resources, writing – review & editing. Jari T. T. Leskinen: investigation, methodology. Vesa-Pekka Lehto: funding acquisition, resources, supervision. Polina Kuzhir: conceptualization, funding acquisition, methodology, resources, supervision.

Conflicts of interest

There are no conflicts to declare.

Data availability

Data for this article, including XRD patterns, XPS spectra, N_2 adsorption–desorption isotherms, EPR spectra, and cyclic voltammograms are available at Zenodo at https://doi.org/10.5281/zenodo.17200691.

Supplementary information (SI): high-resolution TEM images, assignment of XRD reflexes, fluorescence and absorption spectra,

RhB photodegradation kinetics, Tafel plots, linear sweep voltammograms recorded on an RDE, cyclic voltammograms with prolonged cycling, and potentiostatic chronoamperometry curves. See DOI: https://doi.org/10.1039/d5lf00304k

Acknowledgements

This work was supported by the Research Council of Finland (Flagship Programme PREIN, decision 368653 and research projects decision 338733 and 357033) and the Horizon Europe MSCA FLORIN Project 101086142. This research and Nikita Belko were supported by EU Horizon Europe under the Marie Skłodowska-Curie COFUND grant No 101081327 YUFE4Postdocs. The Pohjois-Savon Liitto DeepSurface projects (A78280 & A78303) support is acknowledged for XPS instrument acquisition and measurements. TEM measurements were performed using the facilities of SIB Labs, the Electron Microscopy Laboratory at the University of Eastern Finland. The authors are thankful to the Computational Spectral Imaging research group of the University of Eastern Finland for providing a light source for photocatalytic measurements.

Notes and references

1 D. Li, H. Lv, Y. Kang, N. M. Markovic and V. R. Stamenkovic, *Annu. Rev. Chem. Biomol. Eng.*, 2016, **7**, 509–532.
2 E. J. Calvo and N. Mozhzhukhina, *Electrochem. Commun.*, 2013, **31**, 56–58.
3 J. Qin, Y. Zhang, D. Leng and F. Yin, *Sci. Rep.*, 2020, **10**, 14837.
4 H. Erikson, R. M. Antoniassi, J. Solla-Gulln, R. M. Torresi, K. Tammeveski and J. M. Feliu, *Electrochim. Acta*, 2022, **403**, 139631.
5 M. Shao, Q. Chang, J. P. Dodelet and R. Chenitz, *Chem. Rev.*, 2016, **116**, 3594–3657.
6 S. Hussain, H. Erikson, N. Kongi, A. Sarapuu, J. Solla-Gulln, G. Maia, A. M. Kannan, N. Alonso-Vante and K. Tammeveski, *Int. J. Hydrogen Energy*, 2020, **45**, 31775–31797.
7 A. Bonnefont, A. S. Ryabova, T. Schott, G. Kéranguéven, S. Y. Istomin, E. V. Antipov and E. R. Savinova, *Curr. Opin. Electrochem.*, 2019, **14**, 23–31.
8 S. Trasatti, *Interfacial electrochemistry*, Routledge, 2017, pp. 769–792.
9 Y. Xue, S. Sun, Q. Wang, Z. Dong and Z. Liu, *J. Mater. Chem. A*, 2018, **6**, 10596–10626.
10 S. M. Woo, H. S. Kim, P. J. Youn, K. R. Lee, G. M. Kang, S. H. You, K. S. Lee, Y. T. Kim, S. H. Yu, J. H. Han, S. J. Yoo and I. K. Park, *Chem. Eng. J.*, 2025, **505**, 159586.
11 K. Zhang, H. Dong, W. Dai, X. Meng, H. Lu, T. Wu and X. Zhang, *Anal. Chem.*, 2017, **89**, 648–655.
12 Y. Yang, Y. Ji, G. Li, Y. Li, B. Jia, J. Yan, T. Ma and S. Liu, *Angew. Chem., Int. Ed.*, 2021, **60**, 26790–26797.
13 S. C. Lemos, E. Nossol, J. L. Ferrari, E. O. Gomes, J. Andres, L. Gracia, I. Sorribes and R. C. Lima, *Inorg. Chem.*, 2019, **58**, 11738–11750.
14 J. Wu, Y. Han, Y. Bai, X. Wang, Y. Zhou, W. Zhu, T. He, Y. Wang, H. Huang, Y. Liu and Z. Kang, *Adv. Funct. Mater.*, 2022, **32**, 2203647.
15 X. Chen, W. Zhang, L. Zhang, L. Feng, C. Zhang, J. Jiang and H. Wang, *ACS Appl. Mater. Interfaces*, 2021, **13**, 25868–25878.
16 J. Liu, J. Ke, D. Li, H. Sun, P. Liang, X. Duan, W. Tian, M. O. Tade, S. Liu and S. Wang, *ACS Appl. Mater. Interfaces*, 2017, **9**, 11678–11688.
17 R. Qi, M. Liang, Z. Miao, H. Xu, Y. Fan, J. Mu, W. Feng, L. Diao, J. Zhou, X. Li and T. Ma, *Adv. Funct. Mater.*, 2025, e10948.
18 B. Wulan, X. Cao, D. Tan, J. Ma and J. Zhang, *Adv. Funct. Mater.*, 2023, **33**, 2209114.
19 Y. Ye, Y. Liu, Z. Li, X. Zou, H. Wu and S. Lin, *J. Colloid Interface Sci.*, 2021, **586**, 528–537.
20 M. G. Kim, J. Jeong, Y. Choi, J. Park, E. Park, C. H. Cheon, N. K. Kim, B. K. Min and W. Kim, *ACS Appl. Mater. Interfaces*, 2020, **12**, 11890–11897.
21 W. Li, S. Gao, C. Yang, J. Yang, A. Nisar, G. Xiang and J. Jin, *Nano Res.*, 2024, **17**, 5031–5039.
22 H. Xu, Y. Wang, X. Dong, N. Zheng, H. Ma and X. Zhang, *Appl. Catal., B*, 2019, **257**, 117932.
23 Z. Li, P. Zhang, T. Shao and X. Li, *Appl. Catal., B*, 2012, **125**, 350–357.
24 Z. Li, P. Zhang, T. Shao, J. Wang, L. Jin and X. Li, *J. Hazard. Mater.*, 2013, **260**, 40–46.
25 M. Shao, H. Chen, M. Shen and W. Chen, *Colloids Surf., A*, 2017, **529**, 503–507.
26 Y. Sun, Q. Zhu, B. Bai, Y. Li and C. He, *Chem. Eng. J.*, 2020, **390**, 124518.
27 J. Gan, X. Lu, J. Wu, S. Xie, T. Zhai, M. Yu, Z. Zhang, Y. Mao, S. C. I. Wang, Y. Shen and Y. Tong, *Sci. Rep.*, 2013, **3**, 1021.
28 P. Chang, Y. Wang, Y. Wang and Y. Zhu, *Chem. Eng. J.*, 2022, **450**, 137804.
29 J. Li, Y. Qu, Y. Liu and L. Jing, *Sep. Purif. Technol.*, 2025, **354**, 129412.
30 S. Bagheri, Z. A. M. Hir, A. T. Yousefi and S. B. A. Hamid, *Microporous Mesoporous Mater.*, 2015, **218**, 206–222.
31 D. Shchukin, S. Poznyak, A. Kulak and P. Pichat, *J. Photochem. Photobiol., A*, 2004, **162**, 423–430.
32 J. Mu, B. Chen, M. Zhang, Z. Guo, P. Zhang, Z. Zhang, Y. Sun, C. Shao and Y. Liu, *ACS Appl. Mater. Interfaces*, 2012, **4**, 424–430.
33 S. Impemba, G. Provinciali, J. Filippi, C. Salvatici, E. Berretti, S. Caporali, M. Banchelli and M. Caporali, *Int. J. Hydrogen Energy*, 2024, **63**, 896–904.
34 Z. Jiang, D. Jiang, Z. Yan, D. Liu, K. Qian and J. Xie, *Appl. Catal., B*, 2015, **170–171**, 195–205.
35 S. K. Poznyak, D. V. Talapin and A. I. Kulak, *J. Phys. Chem. B*, 2001, **105**, 4816–4823.
36 G. W. An, M. A. Mahadik, G. Piao, W. S. Chae, H. Park, M. Cho, H. S. Chung and J. S. Jang, *Appl. Surf. Sci.*, 2019, **480**, 1–12.
37 H. Maltanava, N. Belko, K. Tamarov, N. M. Kinnunen, P. Nevalainen, M. Zalieckas, R. Karpicz, I. Koshevoy, D. Semenov, S. Suvanto, S. Malykhin, V.-P. Lehto and P. Kuzhir, *Nanoscale Adv.*, 2025, **7**, 5601–5611.
38 M. LLC, *International Center for Diffraction Data*, https://www.icdd.com/.
39 M. Ingelman-Sundberg and I. Johansson, *J. Biol. Chem.*, 1984, **259**, 6447–6458.

40 M. M. Mubarakshina, B. N. Ivanov, I. A. Naydov, W. Hillier, M. R. Badger and A. Krieger-Liszkay, *J. Exp. Bot.*, 2010, **61**, 3577–3587.
41 W. Xing, G. Yin and J. Zhang, *Rotating electrode methods and oxygen reduction electrocatalysts*, Elsevier, 2014.
42 S. Poznyak and A. Kulak, *Electrochim. Acta*, 2000, **45**, 1595–1605.
43 M. Thommes, K. Kaneko, A. V. Neimark, J. P. Olivier, F. Rodriguez-Reinoso, J. Rouquerol and K. S. Sing, *Pure Appl. Chem.*, 2015, **87**, 1051–1069.
44 S. Gligorovski, R. Strekowski, S. Barbati and D. Vione, *Chem. Rev.*, 2015, **115**, 13051–13092.
45 G. R. Buettner, *Free Radical Biol. Med.*, 1987, **3**, 259–303.
46 W. Kim, T. Tachikawa, G. Moon, T. Majima and W. Choi, *Angew. Chem.*, 2014, **126**, 14260–14265.
47 P. S. Priya, P. P. Nandhini, S. Vaishnavi, V. Pavithra, M. H. Almutairi, B. O. Almutairi, S. Arokiyaraj, R. Pachaiappan and J. Arockiaraj, *Comp. Biochem. Physiol., Part C:Toxicol. Pharmacol.*, 2024, **280**, 109898.
48 E. Ovodok, H. Maltanava, S. Poznyak, M. Ivanovskaya, A. Kudlash, N. Scharnagl and J. Tedim, *Mater. Today: Proc.*, 2017, **4**, 11526–11533.
49 G. Marcì, L. Palmisano, A. Sclafani, A. M. Venezia, R. Campostrini, G. Carturan, C. Martin, V. Rives and G. Solana, *J. Chem. Soc., Faraday Trans.*, 1996, **92**, 819–829.
50 J. Yin and H. Cao, *Inorg. Chem.*, 2012, **51**, 6529–6536.
51 X. Qin, L. Jing, G. Tian, Y. Qu and Y. Feng, *J. Hazard. Mater.*, 2009, **172**, 1168–1174.
52 M. Asiltürk, F. Sayılkan, S. Erdemoğlu, M. Akarsu, H. Sayılkan, M. Erdemoğlu and E. Arpaç, *J. Hazard. Mater.*, 2006, **129**, 164–170.
53 C. Xiao, Z. Tan, C. Wang, X. Yang, G. Zhang and H. Pan, *Mater. Res. Bull.*, 2018, **106**, 197–203.
54 M. V. Malashchonak, S. K. Poznyak, E. A. Streltsov, A. I. Kulak, O. V. Korolik and A. V. Mazanik, *Beilstein J. Nanotechnol.*, 2013, **4**, 255–261.